Multiscale Processes Leading to Supercells in the Landfalling Outer Rainbands of Hurricane Katrina (2005)

BENJAMIN W. GREEN, FUQING ZHANG, AND PAUL MARKOWSKI

Department of Meteorology, The Pennsylvania State University, University Park, Pennsylvania

(Manuscript received 14 November 2010, in final form 30 May 2011)

ABSTRACT

Shallow supercells are frequently observed within the outer rainbands—both onshore and offshore—of landfalling tropical cyclones (TCs). Such supercells can produce tornadoes along the coast even when the center of the parent TC is hundreds of kilometers from land, as was the case with Hurricane Katrina (2005). A convection-permitting simulation with 1.5-km grid spacing in the innermost domain is used in conjunction with radar, radiosonde, and surface observations to investigate the multiscale conditions conducive to supercells in the landfalling outer rainbands of Katrina. Several hours before the eye of the TC made landfall, a baroclinic zone developed along the coast; this front strongly influenced the horizontal distributions of cell-relative helicity and CAPE such that the largest values of these parameters were located over land and water, respectively. An example of a tornadic supercell in the outer rainbands of Katrina is examined. This cell intensified just before landfall and spawned a tornado along the coast, demonstrating the ability of baroclinic boundaries to enhance low-level horizontal vorticity and subsequently intensify updraft rotation within passing cells. Farther inland, the tornadic cell weakened rapidly, suggesting the presence of a narrow coastal zone in which both shear and buoyancy are favorable for tornadogenesis.

1. Introduction

Landfalling tropical cyclones (TCs) have long been known to spawn tornadoes (e.g., Malkin and Galway 1953). Through the mid-1970s, research into TC tornadoes was limited to climatological studies. Relative to TC forward motion, the right semicircle (Sadowski 1962) and then the right-front quadrant (Pearson and Sadowski 1965) between 100 and 250 nautical miles (n mi, where 1 n mi = 1852 m) (Smith 1965) from the center were identified as favorable areas for tornadogenesis. However, Hill et al. (1966) looked at the azimuthal distribution of TC tornadoes and found a stronger clustering in the northeast quadrant (with respect to true cardinal direction) than in the right-front quadrant (with respect to TC forward motion). The following year, Hurricane Beulah was responsible for an outbreak of over 100 tornadoes, many of which occurred northeast of the center but in the left-rear quadrant because the TC was moving toward the south (Orton 1970). Novlan and Gray (1974) updated the work of Hill et al. (1966) through 1972 and showed (their Figs. 2 and 4) that the northeast quadrant was the favorable metric. The right-front and northeast quadrants often overlap significantly because most landfalling TCs in the southeastern United States have a northward component of forward motion. In a study of TC tornadoes from 1950 through 2007, Schultz and Cecil (2009) noted a preferred sector between 340° and 120° in the Northern Hemisphere,[1] applicable in both Earth-relative and TC-relative coordinates.

The radial distribution of TC tornadoes has peaks in two distinct regions (e.g., Gentry 1983): tornadoes in the outer rainbands (i.e., >200 km from the center) are much more influenced by the diurnal cycle than those located within the inner core (Schultz and Cecil 2009). Inner-core rotating cells (or better known as vortical hot towers) have been investigated within the framework of TC dynamics (e.g., Hendricks et al. 2004; Montgomery et al. 2006; Fang and Zhang 2010, 2011). Conversely, supercells in the outer rainbands—regardless of the underlying surface type—have been studied through the

Corresponding author address: Dr. Fuqing Zhang, Dept. of Meteorology, The Pennsylvania State University, 503 Walker Bldg., University Park, PA 16802.
E-mail: fzhang@psu.edu

[1] There have been no studies of TC tornadoes in the Southern Hemisphere.

DOI: 10.1175/WAF-D-10-05049.1

lens of midlatitude severe local storms (e.g., McCaul and Weisman 1996; Suzuki et al. 2000; Lee et al. 2008; Baker et al. 2009; Eastin and Link 2009).

Novlan (1973) was among the first to identify strong vertical wind shear as being favorable for TC tornadogenesis and noted the likely importance of the tilting of horizontal vorticity, which was beginning to be appreciated in studies of midlatitude severe convective storms as the source of mesocyclone rotation (e.g., Barnes 1970). The development of such vertical wind shear was attributed initially to postlandfall TC weakening (Novlan and Gray 1974) and then to increased surface friction over land (Gentry 1983). The necessary ingredients for supercells—vertical wind shear and convective available potential energy (CAPE)—will be discussed below within the context of a TC environment.

The veering of winds within the reference frame of a moving convective cell is associated with streamwise vorticity, the tilting of which leads to cyclonic updraft rotation (Davies-Jones 1984). The flux of streamwise vorticity into an updraft (i.e., the vertically integrated product of the streamwise vorticity and cell-relative wind)—the cell-relative environmental helicity[2] (CREH; Eastin and Link 2009)—is well known to be a useful diagnostic quantity for evaluating the likelihood of cyclonic updraft rotation and tornadoes (e.g., Davies-Jones et al. 1990; Davies-Jones 1993; Rasmussen 2003; Thompson et al. 2003). In studies of continental supercell environments in the United States, those associated with significant (F2 or stronger) tornadoes have nearly twice as much 0–1-km CREH as all other supercell environments (e.g., Markowski et al. 2003). Within TCs, the highest values of CREH over both land and water have been found in the right-front quadrant (e.g., Baker et al. 2009); this quadrant preference was explained by McCaul (1991) as an overlay of a vertically sheared TC steering current on top of the primary (tangential) circulation.

In an observational analysis of landfalling TCs, McCaul (1991) found that CAPE (while relatively small compared with typical values in midlatitude continental supercells) was generally confined to the lowest 400 hPa of the troposphere; horizontally, the highest values of CAPE were found in the right-rear quadrant. For TCs far from land, Bogner et al. (2000) reported that CAPE was distributed axisymmetrically with decreasing values toward the center, in agreement with much earlier studies (e.g., Sheets 1969; Frank 1977). However, Hill et al. (1966) noted that convective instability (which they did not quantify) could vary greatly across rainbands due in part to asymmetries caused by midlevel dry-air intrusions; Curtis (2004) demonstrated a strong relationship between such intrusions and significant TC tornado outbreaks.

In the time after McCaul (1987) examined reflectivity data for tornadoes spawned by Hurricane Danny (1985), the United States has installed the Weather Surveillance Radar-1988 Doppler (WSR-88D) network nationwide; this important upgrade has provided radial velocity data for mesocyclone and tornado detection. Numerous TC supercell cases have been studied in the subsequent years, initially for those cells over land (e.g., Spratt et al. 1997; Suzuki et al. 2000; McCaul et al. 2004; Schneider and Sharp 2007). More recently, Doppler radar (both land based and aircraft mounted) has been used to establish the offshore presence of miniature supercells in Hurricane Katrina (Lee et al. 2008), as well as in other TCs (e.g., Rao et al. 2005; Eastin and Link 2009).

In contrast with the abundance of observational studies, few numerical modeling experiments involving TC supercells and tornadoes have been conducted. Idealized simulations by McCaul and Weisman (1996) initiated storms with a warm bubble within a horizontally homogeneous environment derived from a TC tornado proximity sounding. They found that in spite of small CAPE, the strong vertical wind shear present in an inland TC environment allowed shallow but vigorous supercells to form. Mashiko et al. (2009) simulated the outer rainband of a Japanese typhoon, but were more focused on modeling down to the tornado scale (the minimum horizontal grid spacing was 50 m). A recent simulation of an Indian Ocean TC by Akter and Tsuboki (2010) contained supercells in the outer rainbands, as did more idealized simulations by Morin et al. (2010).

For decades, low-level boundaries have been recognized as preferential locations for tornadogenesis [e.g., Maddox et al. (1980) and references therein]. Gentry (1983) estimated that the tilting of horizontal vorticity was the dominant mechanism of vertical vorticity production in TC tornado environments. He argued that in the case of onshore flow from the TC circulation, increased surface friction over land would produce not only large amounts of horizontal vorticity, but also a region of convergence, in a narrow strip along the coastline. A conceptual model presented by Markowski et al. (1998) suggested that low-level inflow moving along the cool side of a thermal boundary could have baroclinically enhanced horizontal vorticity; this hypothesis has been supported by idealized simulations (Atkins et al. 1999). Surface baroclinic zones have been found in the vicinity of multiple TC tornado outbreaks (McCaul et al. 2004; Edwards and Pietrycha 2006) and their existence has been alluded to in other cases (e.g., Baker et al. 2009).

[2] Following recent work (e.g., Molinari and Vollaro 2008; Eastin and Link 2009), ''cell relative'' will be used to refer to a convective cell; ''storm relative'' is meant to refer to the TC as a whole.

This study focuses on the favorability for supercell development along the landfalling outer rainbands of Hurricane Katrina, a historic TC that made its final Gulf Coast landfall at 1500 UTC 29 August 2005 near the border of Louisiana and Mississippi (Knabb et al. 2006). It is hypothesized that although supercells are possible offshore, baroclinic zones generated along the coastline can provide a mechanism for the enhancement of updraft rotation and therefore increase the likelihood of onshore tornadogenesis. A numerical simulation of Katrina is conducted and agrees reasonably well with reality, except there is not a one-to-one relationship on the scale of individual convective cells. Nevertheless, the simulation provides a full three-dimensional dataset at high spatial and temporal resolutions, something that is not possible with radiosonde, Doppler radar, and surface observations. In section 2, methods used for data collection and processing are detailed. Sections 3 and 4 present results on the cell-scale and larger-scale environments, respectively. An extended discussion is found in section 5, followed by a summary and avenues for future research in section 6.

2. Data and methodology

a. Observations

Multiple observational datasets (Fig. 1a) were used in this investigation. *Storm Data* (NCDC 2005) helped determine tornado reports that were associated with Hurricane Katrina. Hourly observations from surface stations and buoys were used for surface mesoanalyses. WSR-88D land-based measurements were taken from Mobile, Alabama (KMOB), and Eglin Air Force Base, Florida (KEVX), for the 24-h period starting at 0000 UTC 29 August. We were provided with the dual-Doppler analysis conducted by Lee et al. (2008). However, such analyses could not be done for the cells that spawned coastal tornadoes because of poor dual-Doppler geometry: the cells were close to the baseline between the two closest radars, which were over 200 km apart anyway.

Thermodynamic and kinematic profile data were obtained from soundings over land and the Gulf of Mexico (hereafter referred to as rawinsondes and dropsondes, respectively). Rawinsondes from Tallahassee, Florida (KTLH), spanned the period between 1800 UTC 28 August and 0600 UTC 29 August in 6-h intervals. The dropsondes were deployed by the National Oceanic and Atmospheric Administration (NOAA) Gulfstream IV during its second mission of 28 August 2005.

b. The WRF simulation

Version 2.2.1 of the Advanced Research core of the Weather Research and Forecasting Model (WRF-ARW; Skamarock et al. 2005) was used for this study. There were four two-way nested model domains (D1–D4) with the grid spacing decreased by factors of 3 from 40.5 to 1.5 km. The coarsest three model domains—with 160 × 120, 253 × 253, and 325 × 325 horizontal grid points in D1, D2, and D3, respectively—were initialized at 2000 UTC 27 August 2005 with a WRF-based ensemble Kalman filter [EnKF; Meng and Zhang (2008a,b)] that assimilated four legs of Doppler radar velocity observations collected by a NOAA P3 flight mission from 1500 to 2000 UTC following the methodology of Weng and

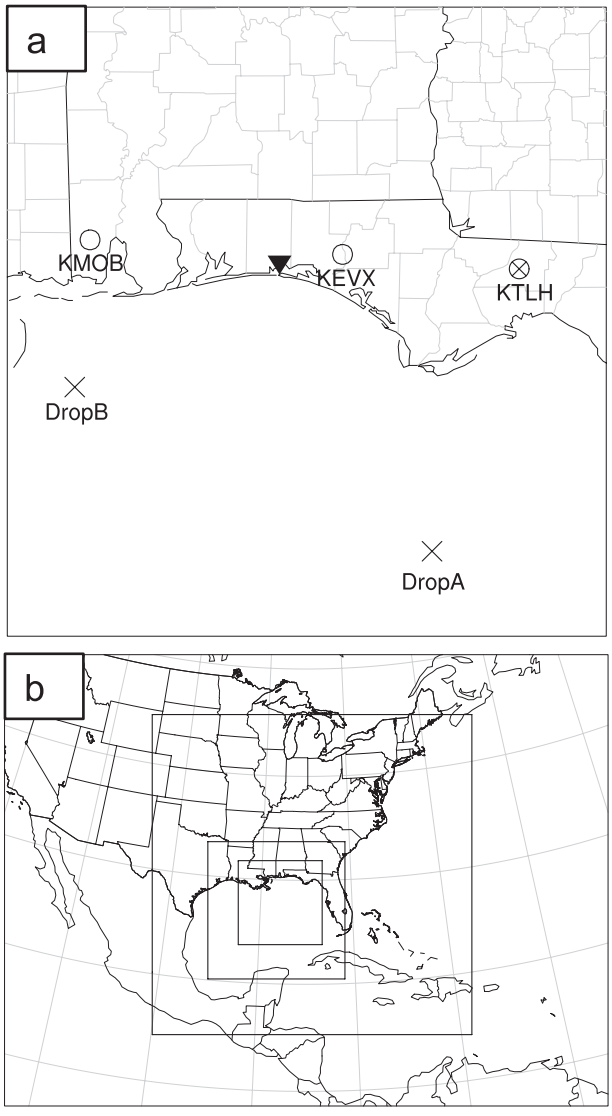

FIG. 1. (a) Locations of WSR-88D sites (○), radiosondes (×), and the Valparaiso tornado (▼). KTLH, for which both radar and rawinsonde data are available, is marked by a circled ×. Annotations are the same as in the main text. (b) Configuration of the WRF domains for the last 24 h of the model integration that is used for all diagnoses in the current study.

Zhang (2012, hereafter WZ). Initialized directly from interpolation of D3, the 1.5-km D4 initially had 298 × 298 horizontal grid points and, like D2 and D3, was centered at and movable with the TC center using the WRF model vortex-following algorithm until 1200 UTC 28 August. For the last 24 h of model integration until 1200 UTC 29 August, all four model domains were fixed in location. Additionally, D4 was augmented to have 595 × 595 horizontal grid points to ensure ample coverage of Katrina and its landfalling outer rainbands (Fig. 1b). As in WZ, the physical parameterization schemes used for this study include the Grell–Devenyi cumulus scheme (Grell and Devenyi 2002, for D1 only), the WRF single-moment six-class microphysics with graupel scheme (Hong et al. 2004), the thermal diffusion scheme for the land surface, the Monin–Obukhov scheme for the surface layer, and the Yonsei State University (YSU) scheme (Noh et al. 2003) for planetary boundary layer processes.

c. CREH and CAPE calculations

Following Davies-Jones et al. (1990), the formula for CREH between the surface ($z = 0$) and some height ($z = H$) can be written as

$$\text{CREH} = \int_0^H \left[(\overline{v} - c_y)\frac{\partial u}{\partial z} - (\overline{u} - c_x)\frac{\partial v}{\partial z} \right] dz, \quad (1)$$

where $\overline{u}$ ($\overline{v}$) is the mean zonal (meridional) wind between heights z and $z + \Delta z$. Furthermore, c_x (c_y) is the zonal (meridional) component of the cell motion, defined in this study[3] as the mean wind (not pressure weighted[4]) between 0 and 6 km, even though supercell motion deviates from the mean wind [see Bunkers et al. (2000) and references therein]. Nevertheless, in an environment with fast cell motions, such as in the outer rainbands of a TC, the deviatory propagation is relatively small and can be neglected. Additionally, the existing supercell motion predictors (e.g., Ramsay and Doswell 2005) were derived from supercell cases over the Great Plains of the United States.

To standardize helicity calculations across data sources, a vertical spacing and integration step of $\Delta z = 100$ m was employed in (1) for $H = 1$ km. Rawinsonde data were linearly interpolated to Δz levels, which is justifiable because there were no gaps greater than $3\Delta z$ between $z = 0$ and $z = H$. Because the dropsondes reported twice per second (approximately once every 5 or 6 m), their data were subsampled (not interpolated) to quasi-100-m levels. Model output also was interpolated to these desired levels.

CAPE typically is defined as the vertically integrated buoyancy between the level of free convection (LFC) and the equilibrium level (EL) for a lifted parcel that ascends pseudoadiabatically once it reaches saturation. The buoyancy force often is approximated in terms of a virtual temperature departure relative to the virtual temperature of the environment (Doswell and Rasmussen 1994), in which case

$$\text{CAPE} = g\int_{\text{LFC}}^{\text{EL}} \frac{T_v - \overline{T}_v}{\overline{T}_v}\, dz, \quad (2)$$

where T_v ($\overline{T}_v$) is the virtual temperature of the lifted parcel (surrounding environment) and g is the acceleration due to gravity. The LFC and the EL exhibit variations both intersonde (in time and location) and intrasonde (the origin of the lifted parcel). Given such fluctuations in the limits of integration of (2), rawinsondes were not interpolated to fixed-height levels for buoyancy calculations.

3. Characteristics of observed and simulated supercells

a. Rainband and cell features as captured by WSR-88D

Supercells were present in at least two outer rainbands of Katrina. The first rainband (Fig. 2a) spawned three tornadoes rated as F0 on the Fujita scale, including one that struck Valparaiso, Florida, at 0230 UTC 29 August. This tornado was subjected to additional radar investigation because it was downwind of the KTLH rawinsonde site. The second rainband reached the Gulf Coast a few hours later; although no tornadoes were reported with this band, there were numerous offshore supercells, as revealed by single- and dual-Doppler analyses (Lee et al. 2008).

1) VALPARAISO TORNADIC CELL

Four minutes before the tornado was reported in Valparaiso, the base reflectivity field of the parent supercell

[3] To determine the sensitivity of helicity to various techniques of calculating cell motion, the modified Bunkers technique (Ramsay and Doswell 2005) was also tested. While the magnitude generally increased, there was no distinguishable change in the spatial pattern of the CREH distribution.

[4] Molinari and Vollaro (2008) demonstrated that defining the cell motion as the pressure-weighted 0–6-km mean wind [as was done by McCaul (1991)] would yield a conservative estimate of CREH. However, because the pressure at $z = 6$ km is not constant over time or space, it was much simpler (especially for the large number of grid points in D4) to calculate the arithmetic mean between $z = 0$ and 6 km as opposed to the integration necessary to obtain the pressure-weighted mean wind.

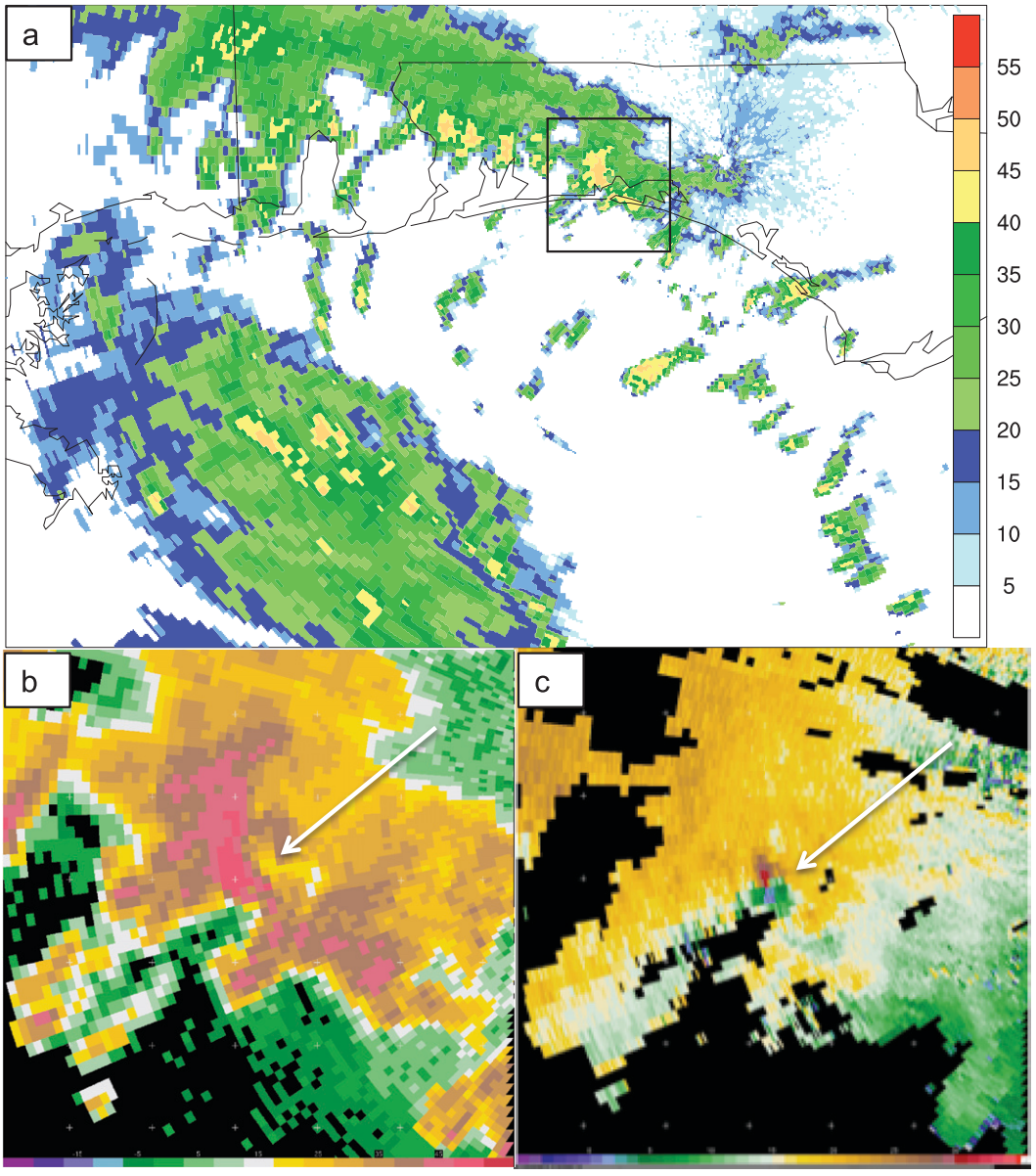

FIG. 2. (a) Long-range base reflectivity (dBZ) from the KEVX WSR-88D at 0226 UTC 29 Aug 2005, 4 min before the Valparaiso tornado was reported. The black box in (a) denotes the domains of (b) base reflectivity (color shaded every 5 dBZ) and (c) base velocity (color bar centered on 15 m s^{-1} with intervals of 1 m s^{-1}). In (b) and (c), the arrows indicate the tornadic cell, and the white tick marks are in 10-km intervals.

(as seen from KEVX; Fig. 2b) did not contain the hook echo that is characteristic of most supercells (very likely owing to numerous neighboring cells), although strong cyclonic azimuthal wind shear was evident in the radial velocity field (Fig. 2c). In terms of radar-derived parameters such as cell top [maximum height of the 30-dBZ echo reflectivity (Maddox et al. 1999)] and vertically integrated liquid (VIL), the cell strengthened over the Gulf of Mexico (Fig. 3). Once the cell reached the mainland, its VIL decreased much more rapidly than the top height. The legacy mesocyclone (M) algorithm (NOAA 2006) classified the tornadic cell as a mesocyclone between 0205 and 0226 UTC (Table 1), and a tornado vortex signature was detected at 0218 UTC. The measured horizontal shear doubled between consecutive scans as the cell crossed from the open waters of the Gulf of Mexico onto a barrier island. The mesocyclone weakened just as rapidly as it intensified: at 0226 UTC, the cell's most intense rotation was the closest to the ground thus far—2200 ft or 670 m (cf. Fig. 2c)—and was near peak intensity, yet

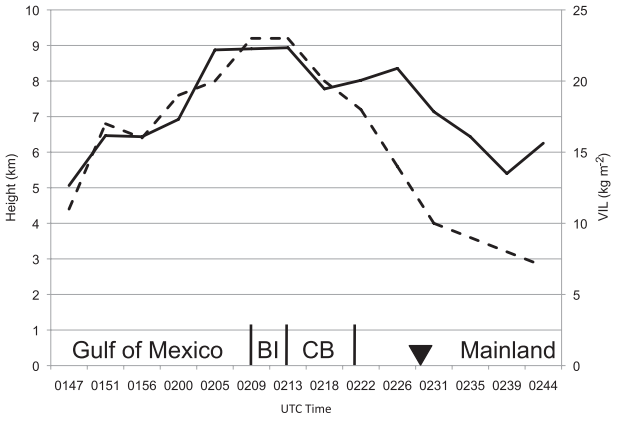

FIG. 3. Temporal evolution of cell top (solid line) and VIL (dashed line) for the tornadic cell between 0147 and 0244 UTC 29 Aug, as derived by the KEVX WSR-88D. The cell was located over the Gulf of Mexico until approximately 0210 UTC, then briefly crossed a barrier island (BI) and Choctawhatchee Bay (CB) before reaching the mainland around 0220 UTC. The filled triangle denotes the time of the tornado report (0230 UTC).

TABLE 1. Temporal evolution of legacy M parameters for the cell that spawned a tornado at Valparaiso at 0230 UTC 29 Aug 2005 (refer to text).

Time (UTC)	Top height of mesocyclone (ft)	Max shear (10^{-3} s^{-1})	Height of max shear (ft)	Range to radar (n mi)
0205	8400	9	4100	26
0209	5200	8	3100	27
0213	5400	16	4400	28
0218*	5500	14	5500	29
0222	7700	10	3500	30
0226	3700	15	2200	32

* A tornado vortex signature was detected at this time.

at 0231 UTC the M algorithm could not detect a mesocyclone and there was no sign of a base velocity couplet (not shown).

2) NONTORNADIC SUPERCELLS

The authors of Lee et al. (2008) generously provided their dual-Doppler analysis, which used the data from the Slidell, Louisiana (KLIX), and KMOB radars at 0604 UTC 29 August. Reflectivity, vertical vorticity, and vertical velocity (over the domain of their Fig. 3a) were interpolated to a height of $z = 1.5$ km and plotted in our Fig. 4. The vorticity maximum of the northern supercell ["mesocyclone 12" in Lee et al. (2008)] was collocated with the main updraft, which was surrounded by weaker downdrafts. The southern cell (their mesocyclone 13) had two updrafts of nearly equal strength with a downdraft (magnitude < 1 m s^{-1}) at the reflectivity maximum, which suggests cell weakening. Several characteristics of these observed supercells also were present in supercells generated by the WRF simulation.

b. An example supercell in the numerical simulation

Because innumerable convective cells were present within the simulated TC at any given time, an objective parameter was necessary to identify supercells. Although often used to identify continental supercells, updraft helicity (Kain et al. 2008) proved to be a poor metric in this instance because the outer rainband cells were tilted and shallow. In lieu of updraft helicity, a possible supercell is identified if its low-level ($z = 1.5$ km) rotating updraft exceeds vorticity and velocity thresholds of 0.005 s^{-1} and 1.0 m s^{-1}, respectively, for at least 24 min (model output in D4 was saved every 6 min). A time-lapse plot of cells that met these criteria (Fig. 5a) clearly shows organized rainbands spiraling around the TC center, as well as a secondary cluster of rotating updrafts in the vicinity of the coast. Only these coastal cells were examined in more detail for comparison with the limited observations presented in the previous subsection.

1) GENERAL CHARACTERISTICS

The example supercell was tracked between model times 0248 and 0342 UTC 29 August as it paralleled the coast and made landfall in southeastern Louisiana (Figs. 5b and 5c). This cell developed just to the south of an existing convective cell; at 0300 UTC (top halves of Figs. 6 and 7), the updraft, which exceeded 13 m s^{-1} between $z = 4$ km and $z = 5$ km, straddled a cyclonic–anticyclonic vortex couplet. The cell structure changed dramatically by 0324 UTC (bottom halves of Figs. 6 and 7), as the primary updraft maximum at $z = 1.5$ km was nearly coincident with the strongest vorticity at $z = 2$ km. The presence of a secondary updraft maximum (located here at a height of 5 km) has been observed in a recent study of offshore supercells in Hurricane Ivan (Eastin and Link 2009) and in a simulation made from a tornado-proximity sounding from the remnants of Hurricane Danny [CKL in Fig. 9 of McCaul and Weisman (1996)]. Furthermore, the appearance of dual updrafts on the west and south sides of the cell (Fig. 6d) is remarkably similar to the vertical velocity structure of the observed Mesocyclone 13 (Fig. 4b).

Some features were evident throughout the life of the cell. Weak convective downdrafts generated slowly spreading cold pools. To the south of these cold pools, parcels that were lifted from low levels had CAPE > 500 J kg^{-1}. From before 0300 UTC (not shown) through 0324 UTC, the fraction of cell-relative inflow in the lowest 1 km that was from the north increased. Thus, the updraft started to ingest air that was more dense (i.e., air with lower virtual potential temperature θ_v) but rich in cell-relative streamwise vorticity (Figs. 6b and 6d).

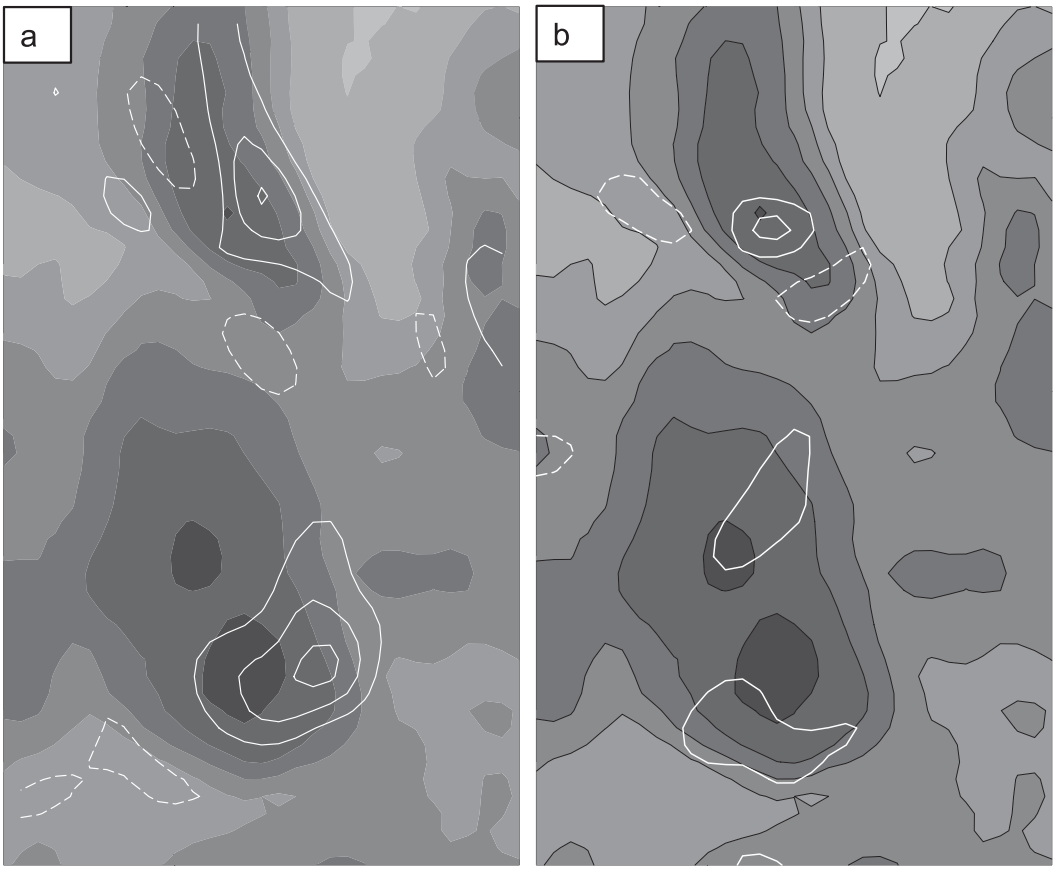

FIG. 4. KLIX and KMOB dual-Doppler analysis at 0604 UTC 29 Aug, provided by the authors of Lee et al. (2008) and interpolated to a height of $z = 1.5$ km. Reflectivity is shaded every 5 dBZ between 20 and 50 dBZ. White contours are of (a) vertical vorticity ζ in intervals of 10^{-3} s^{-1} and (b) vertical velocity w in intervals of 1 m s^{-1}. Zero contours are omitted, and negative contours are dashed.

2) GENERATION OF VERTICAL VORTICITY

The presence of streamwise vorticity on the northern side of the cell prompted an examination into the generation and advection of vertical vorticity ζ. Ideally, a vorticity budget should be calculated within a Lagrangian framework (e.g., Atkins et al. 1999), but the combination of the relatively coarse grid spacing (1500 m), somewhat infrequent[5] output time step (360 s), and strong grid-relative cell motion (>20 m s^{-1}) limited the calculations to an Eulerian framework. That the Eulerian formulation only diagnoses instantaneous forcings cannot be stressed enough. After neglecting the baroclinic, Coriolis, and frictional contributions to ζ, the vertical component of the vorticity equation can be written as [see Eq. (2) of Eastin and Link (2009)]

$$\frac{\partial \zeta}{\partial t} = -\mathbf{v}_h \cdot \nabla_h \zeta - w\frac{\partial \zeta}{\partial z} - \zeta(\nabla_h \cdot \mathbf{v}_h) - \left(\frac{\partial w}{\partial x}\frac{\partial v}{\partial z} - \frac{\partial w}{\partial y}\frac{\partial u}{\partial z}\right), \quad (3)$$

where $\mathbf{v}_h$ and ∇_h are the horizontal components of the (cell relative) wind and of the gradient operator, respectively, and w is the vertical velocity. The term on the lhs of (3) is the local rate of change of ζ. On the rhs, the first term (VHAD) is the horizontal advection of ζ by the cell-relative winds and the second term (VVAD) is the vertical advection of ζ. The third term (VCON) represents the generation of ζ by convergence or stretching. The tilting of horizontal vorticity into the vertical is included as the last term (VTIL).

The terms on the rhs of (3) were computed in the vicinity of the example supercell at 0300 UTC. At $z = 2$ km (Fig. 8), positive contributions from convergence and tilting were located within the developing vorticity maximum, and a greater contribution from vertical advection was centered on the strongest part of the updraft. The sum

[5] The simulation was performed with the primary intent to examine the performance of WRF-EnKF in making a multiday TC forecast and to examine the structure and dynamics of the inner core of Katrina.

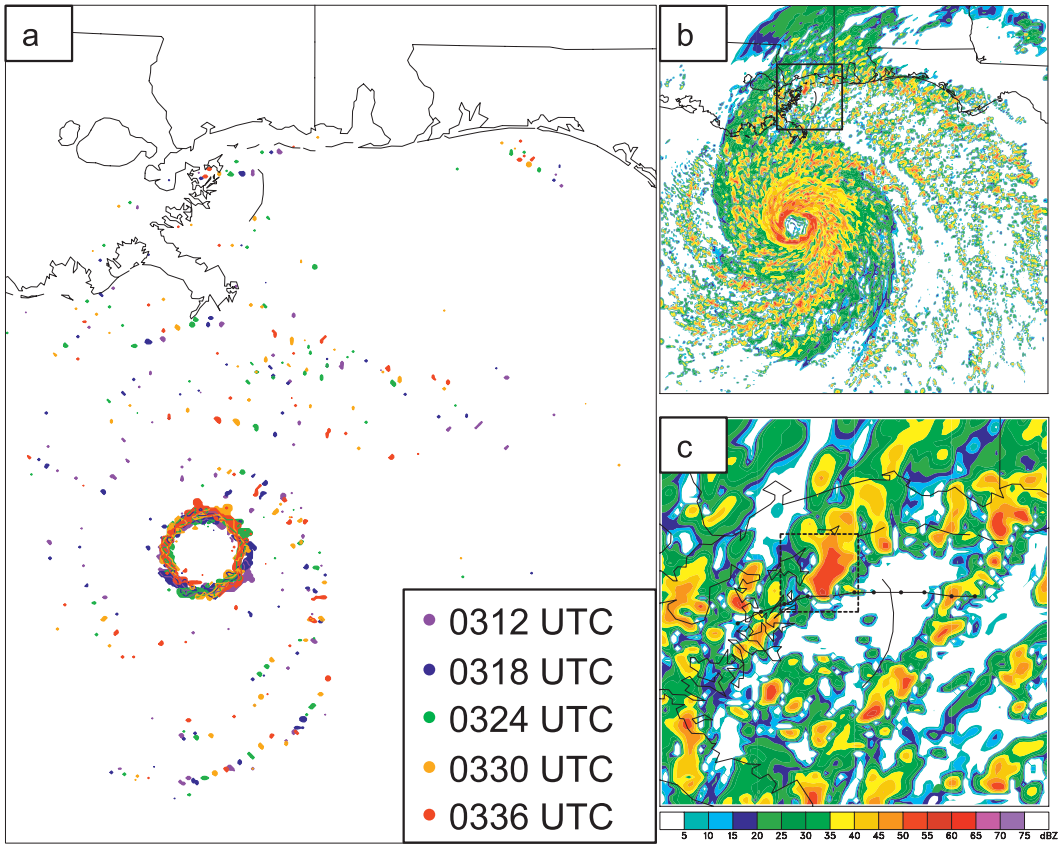

FIG. 5. (a) WRF-simulated (in D4) $w\zeta \geq 0.005$ m s^{-2} subject to $w \geq 1$ m s^{-1} and $\zeta \geq 0.005$ s^{-1} at a height of $z = 1.5$ km, valid from 0312 through 0336 UTC 29 Aug (see color code). (b),(c) WRF-simulated reflectivity at $z = 125$ m, valid 0324 UTC. The entirety of D4 is covered in (b); the black box shows the domain of (c). In (c), the track of the "selected cell" is marked in 6-min intervals by the points along the line. The 35 km × 35 km dashed black box in (c) denotes the location of Figs. 6c and 6d.

of the four terms on the rhs of (3) supports an instantaneous increase of ζ at 0300 UTC (Fig. 8d). Closer to the surface (not shown), tilting was smaller than either convergence or vertical advection. That low-level vorticity in this particular cell appears to have been generated by convergence—and by tilting, to a lesser extent—and then transported to higher levels by the updraft is in agreement with observations of supercells in the offshore outer rainbands of Hurricane Ivan (Eastin and Link 2009). It is worthwhile, however, to examine the environmental processes that govern the life cycle of TC supercells.

4. Environmental influences on TC supercell formation and evolution

a. Observational data

1) SURFACE CONDITIONS NEAR THE COAST

A detailed look at the coastline was motivated by its suspected role in TC tornadogenesis (e.g., Gentry 1983; Baker et al. 2009) and by the identification of coastal fronts ahead of TC landfalls (Knupp et al. 2006; Srock and Bosart 2009). Observations of winds and of θ_v from surface stations and from offshore buoys were plotted to identify baroclinic zones and to study their evolution. A density gradient[6] was present along the Mississippi coast at 0000 UTC 29 August (Fig. 9a). Over the next 3 h, land-based nocturnal cooling allowed the gradient to become more pronounced (Fig. 9b). The kinematic boundary was already well established: offshore, winds followed the large-scale tangential circulation of Katrina whereas onshore, increased surface friction caused the winds to decelerate and turn back toward low pressure (Baker

[6] The best way to identify horizontal buoyancy gradients is to use the density potential temperature θ_ρ (defined as in Emanuel 1994, p. 161), which accounts for the effects of hydrometeor loading. Given the challenges associated with obtaining the hydrometeor mass from (radar) observations, we instead calculate θ_v for both observational and simulation data.

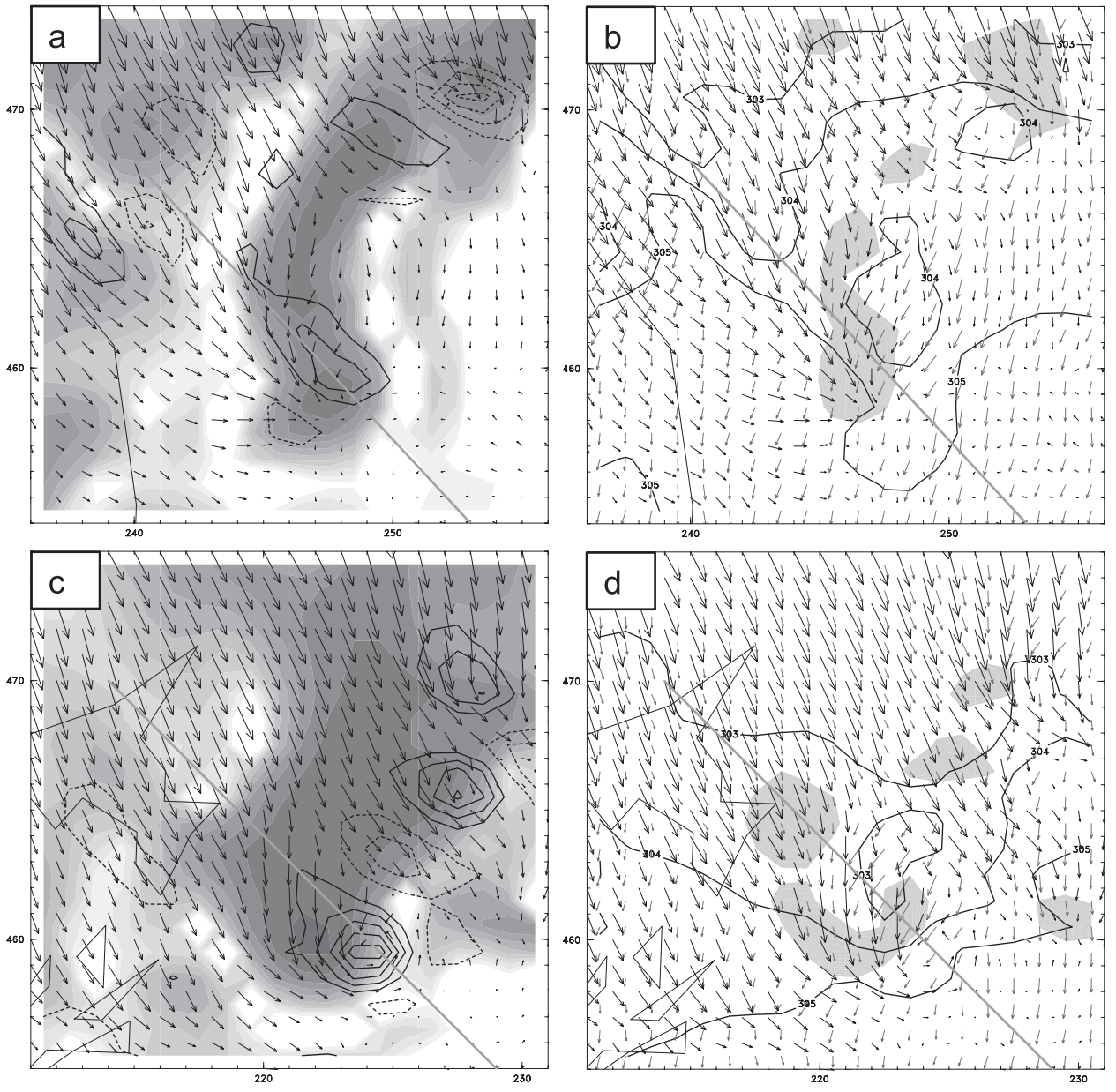

FIG. 6. Plan views of the cell of interest at $z = 125$ m. Tick marks every 1.5 km. Diagonal lines depict cross sections in Fig. 7. (a) Simulated reflectivity > 5 dBZ in intervals of 5 dBZ (shaded), ζ every 10^{-3} s^{-1} (black contours), and cell-relative horizontal winds (black vectors) valid 0300 UTC 29 August. (b) As in (a), but for virtual potential temperature $\theta_v \leq 305$ K each 1 K (black contours) and horizontal vorticity (gray vectors). (c),(d) As in (a),(b), respectively, but valid at 0324 UTC. Gray shading in (b) and (d) indicates where $w > 2$ m s^{-1} at a height of $z = 1.5$ km. Zero contours are omitted, and negative contours are dashed.

et al. 2009). The resultant zone of confluence and mass convergence along the coastline is in excellent agreement with prior studies (e.g., Powell 1982; Gentry 1983). Unfortunately, such a dense network of observations does not extend above the surface. Nevertheless, there were some notable differences between rawinsondes launched over land and dropsondes deployed over the Gulf of Mexico.

2) RADIOSONDES

KTLH was chosen as the representative rawinsonde location because it was closest to the Valparaiso tornadic cell (approximately 220 km)[7] and within 50 km of

[7] Note that Novlan and Gray (1974) defined a proximity sounding as being within 185 km and 3 h of the tornado report.

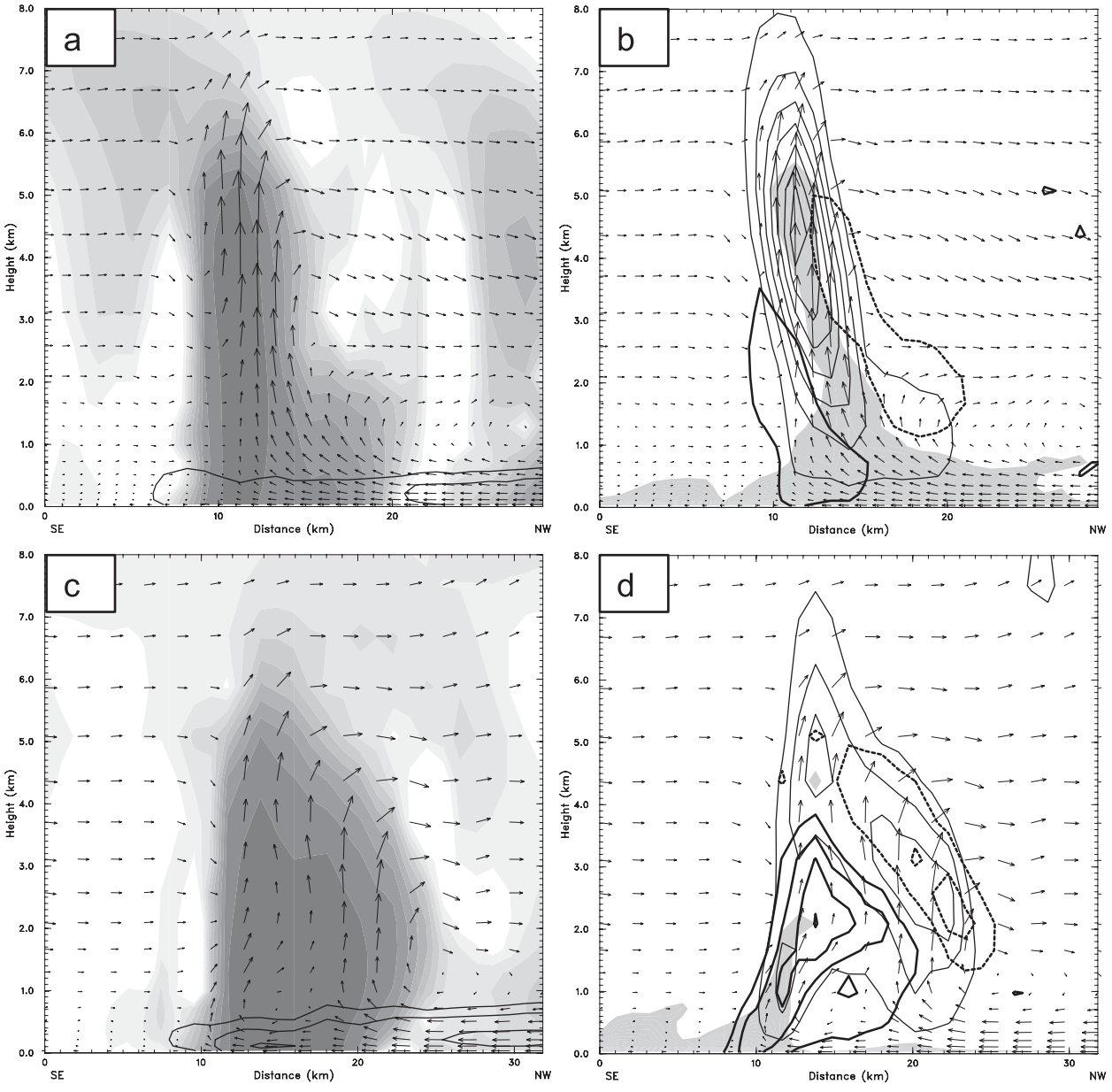

FIG. 7. Southeast–northwest vertical cross sections of the cell of interest. (a) Simulated dBZ (as in Fig. 6), $\theta_v \leq 305$ K each 1 K (black contours), and cell-relative three-dimensional circulation (vectors) valid 0300 UTC 29 Aug (cf. Figures 6a,b). (b) As in (a), but for ζ each 0.002 s^{-1} (heavy black contours) and w at $1, 3, 5, \ldots, 15$ m s^{-1} (thin black contours). Light gray fill indicates a parcel lifted from that level would have CAPE ≥ 500 J kg^{-1}. (c),(d) As in (a),(b), respectively, but valid at 0324 UTC (cf. Figs. 6c and 6d). Zero contours are omitted, and negative contours are dashed.

the coast (refer to Fig. 1a). Although the center of Katrina was between 570 and 600 km to the south and west of KTLH, the influence of the TC was evident at 0000 and 0600 UTC 29 August (Figs. 10a and 10b). Calculations of surface-based CAPE and 0–1-km CREH for all radiosondes are provided in Table 2.

Despite large CAPE at 0000 UTC, the relatively small low-level helicity meant that the environment was unfavorable for significant updraft rotation (Davies-Jones 1984). A shallow nocturnal inversion developed over the following 6 h, decoupling the mixed layer from the ground (decreasing surface-based CAPE) and reducing the depth of the frictional layer (increasing 0–1-km CREH). Although the CAPE at 0600 UTC was similar to that of the average TC tornado sounding used by McCaul and Weisman (1996), the ability to sustain

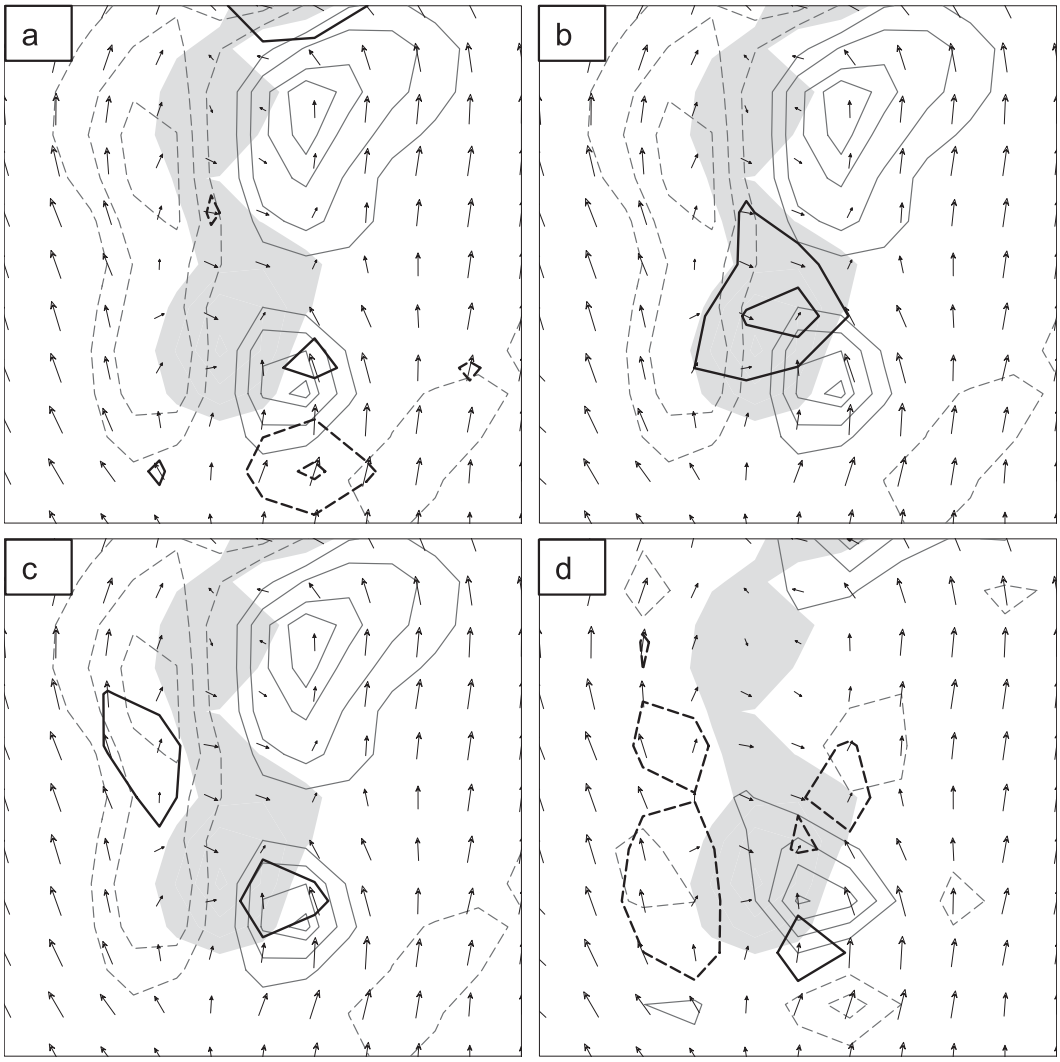

FIG. 8. WRF-simulated forcing terms of the rhs of Eq. (3), valid 0300 UTC 29 Aug at a height of $z = 2$ km. (a) Cell-relative VHAD, (b) VVAD, (c) VCON, and (d) VTIL (black contours) every 5×10^{-6} s^{-2}. Cell-relative horizontal winds (vectors) and $w > 2$ m s^{-1} (gray fill) are plotted in all panels. In (a)–(c) ζ (gray contours) is shown every 10^{-3} s^{-1}, whereas the gray contours in (d) depict the sum of the rhs of (3)—i.e., VHAD + VVAD + VCON + VTIL—shown every 5×10^{-6} s^{-2}. Zero contours are omitted, and negative contours are dashed.

surface-based supercells in the presence of a (deeper) cold layer is questionable (e.g., Maddox et al. 1980).

For the investigation of the offshore environment around Katrina's prominent outer band, ideal dropsondes would have been deployed near the coast in the hours preceding the rainband landfall. The dropsondes that best fit these criteria were deployed (Fig. 1a) at 1741 and 1806 UTC 28 August (hereafter referred to as "DropA" and "DropB" respectively). Visual inspection of visible and water vapor satellite imagery (not shown) indicated that DropA (Fig. 10c) sampled a region of relatively dry air on the eastern periphery of Katrina and that DropB (Fig. 10d) was situated between the two outermost rainbands. Although CAPE exceeded 1300 J kg^{-1} in both sondes (Table 2), DropB—located closer to the coast and the TC center—had significantly more low-level helicity. The environmental conditions within the offshore outer rainbands of Katrina favored supercells: indeed, they were observed [see Fig. 3 of Lee et al. (2008) and Fig. 4 of this manuscript].

b. Simulated environment

A numerical simulation can be used to investigate phenomena that cannot be resolved by observational networks, provided that there is reasonable agreement between the two.

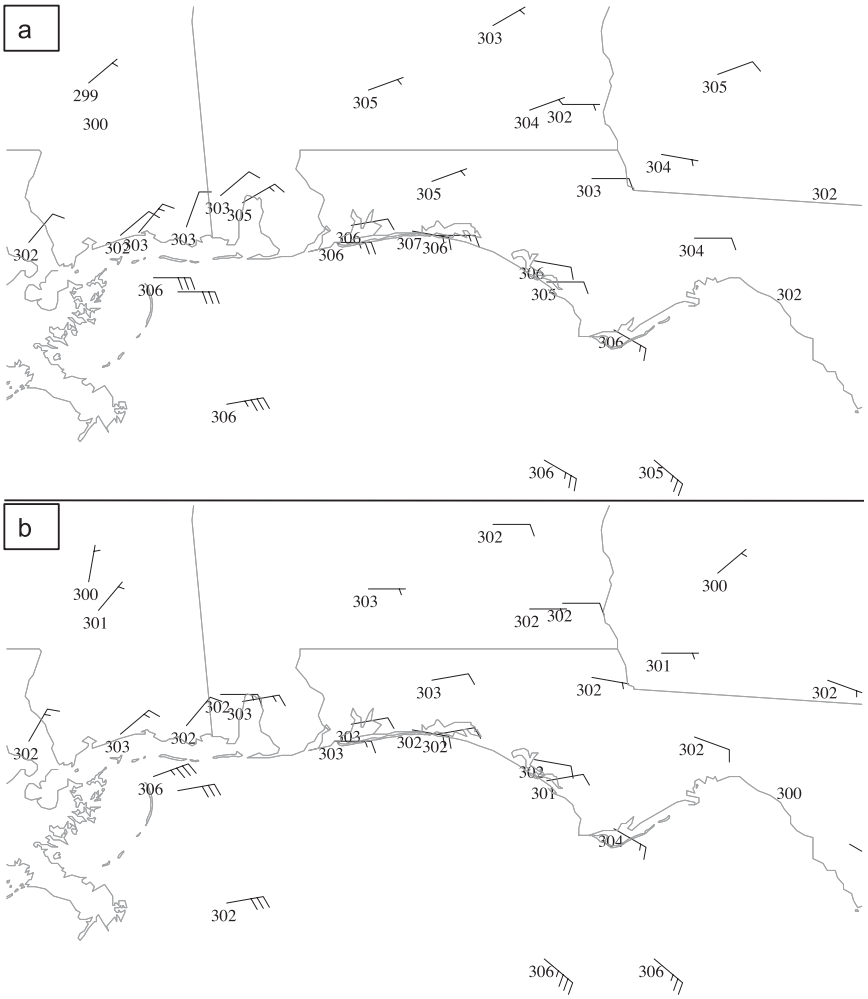

FIG. 9. Surface observations of θ_v (K) and winds (full barb = 10 kt, where 1 kt = 0.514 m s^{-1}) at (a) 0000 and (b) 0300 UTC 29 Aug.

1) MODEL-GENERATED COASTAL FRONT

A shallow coastal front was evident in the simulation even after using a Cressman (1959) smoother with a 22.5-km radius of influence to remove the localized effects of individual convective cells (Fig. 11b). This simulated front at 0324 UTC was similar to the observed front at 0300 UTC (Fig. 9b): in both, there was mass convergence along the coast, and θ_v decreased by ~4 K from water to land. The simulation might have exaggerated the strength of the baroclinic zone on 28 August (not shown), although this error is not severe enough to jeopardize the analysis of the coastal front at 0324 UTC.

A cross section (Fig. 11a) shows that a strong gradient of θ_v in the lowest 1 km coincided with an area of confluence; note the northeasterly (southeasterly) winds onshore (offshore). In addition, a westward-moving cell (different than the example supercell discussed previously) passed 10 km to the south of the coastal front. Notable decreases in low-level values of CAPE[8] and θ_v at the 40-km mark of the cross section indicate that the cell-generated cold pool was somewhat separate from the background baroclinic zone. Inspection of the same cross section for the next few time steps (not shown) revealed an appreciable recovery of near-surface air in the wake of the cell through the combined effects of oceanic heat fluxes and strong horizontal advection.

We were interested in the mechanisms that formed the coastal baroclinic zone. In terms of θ_v, surface

[8] For a particular vertical level in cross-section plots (e.g., Figs. 7b, 7d, 11a), CAPE is calculated by assuming a parcel is lifted from that level.

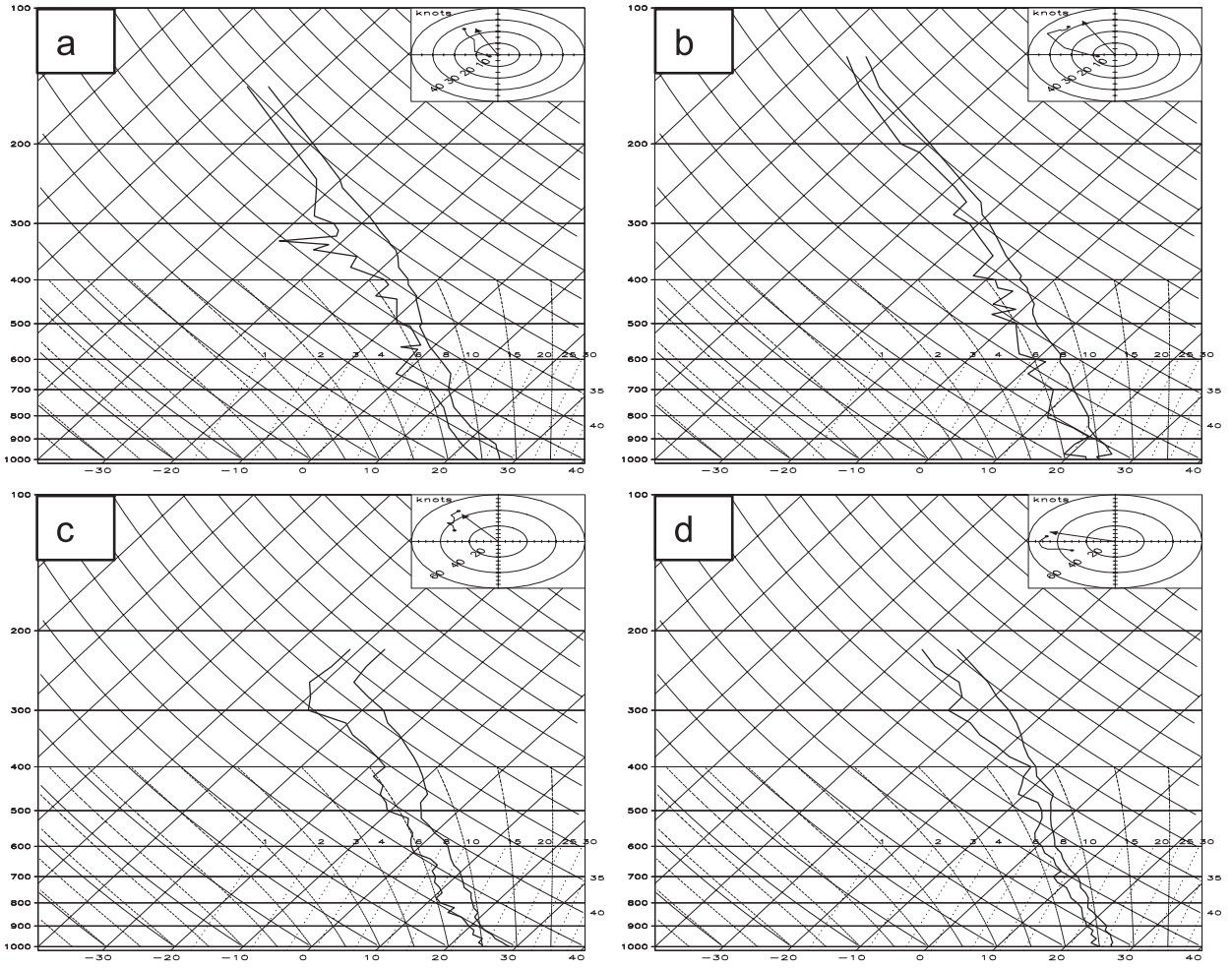

FIG. 10. Skew *T* plots of KTLH rawinsondes at (a) 0000 and (b) 0600 UTC 29 Aug, and of (c) DropA at 1741 UTC 28 Aug and (d) DropB at 1806 UTC 28 Aug. Hodograph traces are between the surface and a height of approximately 1 km.

frontogenesis can be written in a form similar to Eq. (2.3.21) of Bluestein (1993) as

$$\frac{d}{dt}|\nabla_h\theta_v| = |\nabla_h\theta_v|^{-1}(\text{FDEF} + \text{FTIL} + \text{FDIA}), \quad (4)$$

where

$$\text{FDEF} = -\frac{\partial u}{\partial x}\left(\frac{\partial\theta_v}{\partial x}\right)^2 - \frac{\partial v}{\partial y}\left(\frac{\partial\theta_v}{\partial y}\right)^2 - \left(\frac{\partial\theta_v}{\partial x}\frac{\partial\theta_v}{\partial y}\right)\left(\frac{\partial v}{\partial x} + \frac{\partial u}{\partial y}\right), \quad (5)$$

$$\text{FTIL} = -\frac{\partial\theta_v}{\partial z}\left(\frac{\partial w}{\partial x}\frac{\partial\theta_v}{\partial x} + \frac{\partial w}{\partial y}\frac{\partial\theta_v}{\partial y}\right), \quad \text{and} \quad (6)$$

$$\text{FDIA} = \frac{\partial\theta_v}{\partial x}\frac{\partial}{\partial x}\left(\frac{d\theta_v}{dt}\right) + \frac{\partial\theta_v}{\partial y}\frac{\partial}{\partial y}\left(\frac{d\theta_v}{dt}\right) \quad (7)$$

are the horizontal deformation, vertical tilting, and diabatic terms, respectively. Plots of (4)–(7) along the coastline (Fig. 12) reveal that FDEF—the first two terms in (5) in particular (not shown)—was responsible

TABLE 2. Computed surface-based CAPE and 0–1-km CREH for rawinsondes and dropsondes deployed near the northern coast of the Gulf of Mexico in the hours leading up to Hurricane Katrina's landfall. The composite TC tornado sounding (AVG) from McCaul and Weisman (1996) is provided for reference.

Profile	CAPE (J kg^{-1})	0–1-km CREH (m^2 s^{-2})
KTLH (0000 UTC 29 Aug)	1842	54
KTLH (0600 UTC 29 Aug)	592	201
DropA (1741 UTC 28 Aug)	2173	69
DropB (1806 UTC 28 Aug)	1336	152
McCaul and Weisman (1996) composite (AVG)	619	149*

* This is the 0–3-km CREH because McCaul and Weisman (1996) did not calculate the 0–1-km CREH.

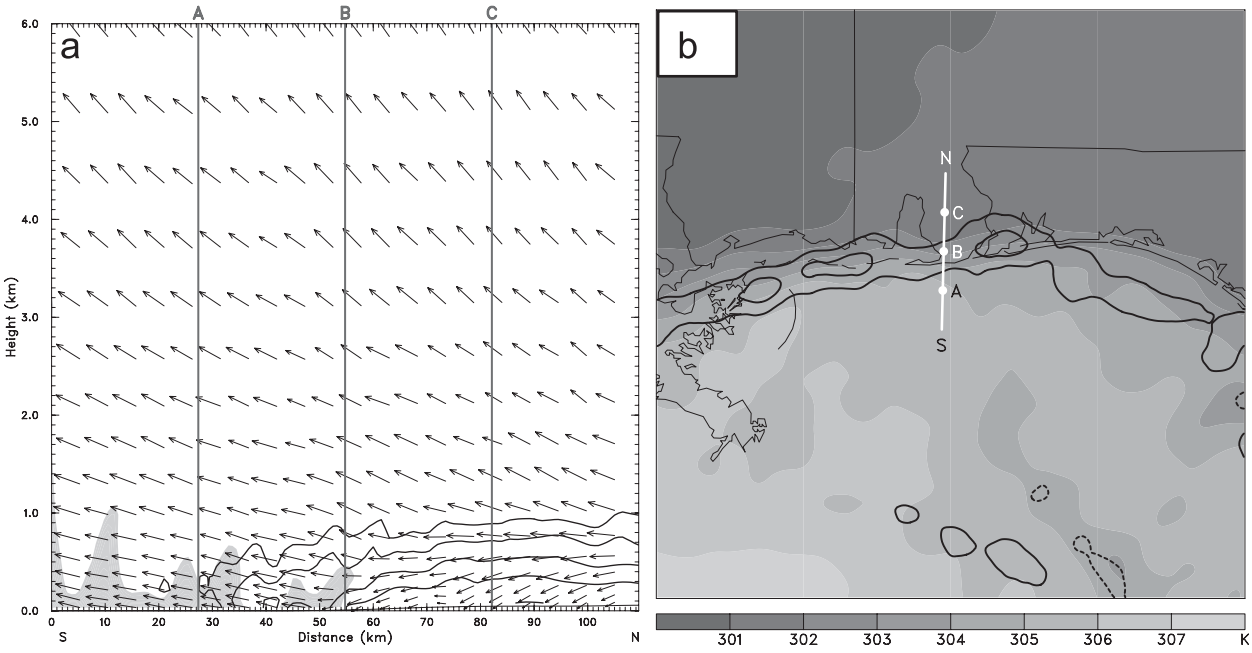

FIG. 11. Simulated coastal environment, valid 0324 UTC 29 Aug. CAPE and 0–1-km CREH values are given in Table 3 for the points marked by A–C. (a) Meridional cross section (approximately 110 km in length) across the coastline. CAPE $\geq$ 500 J kg^{-1} is filled gray as in Fig. 7. Shown is θ_v (black contours) every 1 K for $\theta_v \leq 305$ K; vectors represent vertical profiles (i.e., not circulation vectors) of the ground-relative horizontal wind. (b) Plan view of surface θ_v (shaded) and convergence at $z = 125$ m (black contours) every 2×10^{-4} s^{-1}; both fields were smoothed using a Cressman (1959) weighting function with a horizontal radius of influence of 22.5 km. The white line between points S and N represents the south–north cross section in (a). Zero contours are omitted, and negative contours are dashed.

for frontogenesis, which is consistent with the zone of enhanced confluence (Fig. 11a). Although FDIA was two orders of magnitude smaller than FDEF or FTIL, differential diabatic heating at the surface likely promoted the initial development of the front.

CAPE and 0–1-km CREH values were computed (Table 3) at ~30-km intervals along the cross section (Fig. 11). The dense coverage of convection (e.g., Fig. 5b) made the retrieval of ''representative'' and ''undisturbed'' soundings (which are essential for CAPE calculations) impractical. Despite this constraint, Table 3 is consistent with a coastal baroclinic zone: higher buoyancy offshore and much higher CREH onshore.

2) TC-SCALE ENVIRONMENT

Although the simulation developed a stable boundary layer over land earlier than was actually observed (cf. Table 2 with Fig. 13b), factors other than the underlying surface type that affected the distributions of CAPE (Fig. 13) and CREH (Fig. 14) are in agreement with results from prior studies. For example, CAPE exhibited a generally axisymmetric distribution, consistent with Bogner et al. (2000). CREH on the other hand was considerably larger in the northeast, right-front (McCaul 1991; Baker et al. 2009), and downshear-left[9] (Molinari and Vollaro 2008, 2010) quadrants.

5. Discussion

An abundance of prior research has noted that, due to very large low-level vertical wind shear and sufficient buoyancy, TCs can spawn supercells both onshore (e.g., McCaul 1987, 1991; McCaul and Weisman 1996; Schneider and Sharp 2007) and offshore (e.g., Lee et al. 2008; Baker et al. 2009; Eastin and Link 2009). Here, we further discuss how a TC-generated baroclinic zone can regulate tornadogenesis in landfalling outer rainband supercells and speculate on the importance of dry-air intrusions in supercell formation.

[9] The large-scale 850–200-hPa shear vector across the simulated TC pointed between northeast and east-northeast from 0000 UTC 29 August onward. As the TC was moving to the north-northwest, there was considerable overlap between the northeast, right-front, and downshear-left quadrants.

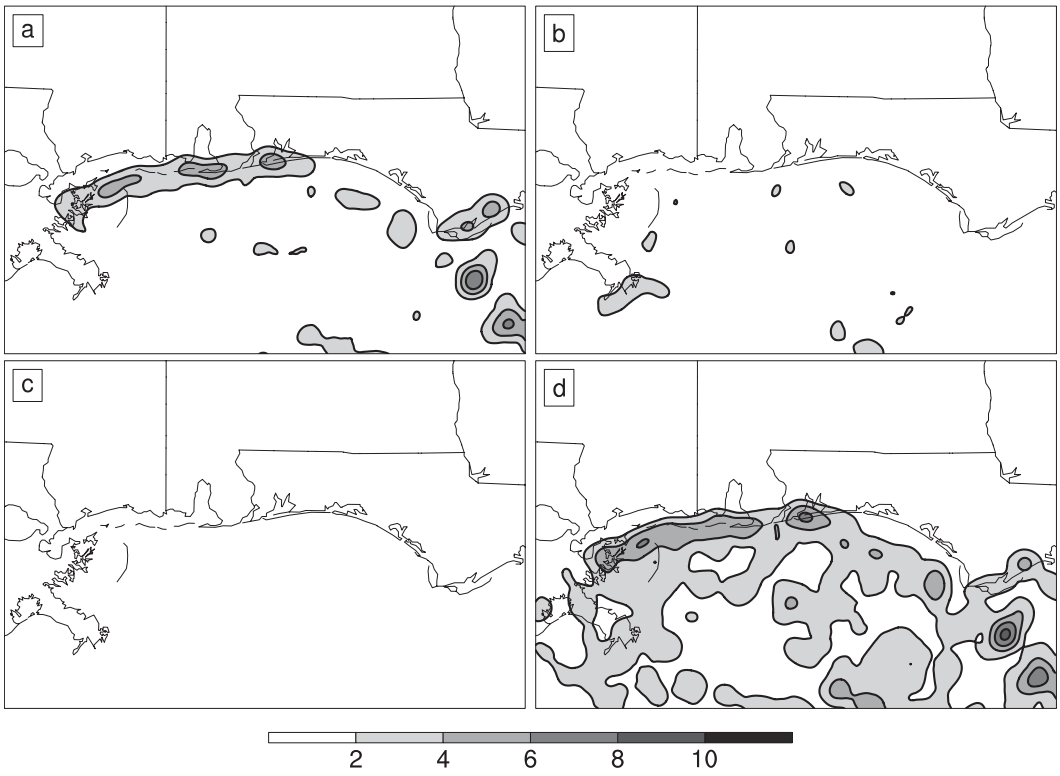

FIG. 12. Simulated surface θ_v frontogenesis [K (10 km)$^{-1}$ h^{-1}] at 0324 UTC 29 Aug for (a) FDEF, (b) FTIL, (c) FDIA, and (d) total frontogenesis. In each panel, the same smoother used in Fig. 11 was applied after all computations, and thus (a)–(c) do not graphically sum to (d). In other words, if * denotes a smoothed field, then the quantity plotted in (d) is (FDEF + FTIL + FDIA)* $\neq$ FDEF* + FTIL* + FDIA*.

a. The coastal baroclinic zone

1) TC-INDUCED COASTAL FRONTOGENESIS

The development of a temperature gradient along the coastline is possible given the different heat capacities of sea and land. Such coastal fronts have been known to interact with landfalling TCs along the eastern United States (e.g., Srock and Bosart 2009). Indeed, both surface observations (Fig. 9) and model output (Fig. 11) indicate that a thermal gradient was present along the coast prior to TC landfall. This boundary initially formed from differential heat fluxes, and intensified over time (Fig. 12) through confluence that arose from differential surface friction (Powell 1982; Gentry 1983). Knupp et al. (2006) presented observational evidence of coastal frontogenesis through these same mechanisms (see their Fig. 9) for the case of Tropical Storm Gabrielle (2001). Coastal baroclinic zones that develop ahead of TC landfall also feature large gradients in kinematic fields (Figs. 9 and 11), including CREH (Fig. 14). Obviously, the presence of a coastal front has major implications for landfalling supercells.

2) IMPACTS ON CELL EVOLUTION AND TORNADOGENESIS

A coastal front that forms ahead of a landfalling TC clearly fits the ''buoyancy limiting'' or ''buoyancy-shear overlapping'' categories of TC tornadoes described by Edwards and Pietrycha (2006). The intersection of favorable shear and buoyancy that occurs along mesoscale boundaries also has been implicated in continental tornadogenesis (e.g., Rasmussen et al. 2000). Offshore, sufficient levels of CAPE and helicity enabled low-level rotating updrafts to develop in the outer rainbands (e.g., Fig. 5a). In agreement with the simulations of Atkins et al. (1999), a supercell that approaches land will

TABLE 3. Simulated surface-based CAPE and 0–1-km CREH for various locations near the coastline at 0324 UTC 29 August. Letters A–C correspond to the points marked in Fig. 11.

Profile	CAPE (J kg^{-1})	0–1-km CREH (m^2 s^{-2})
A	1139	73
B	263	325
C	57	601

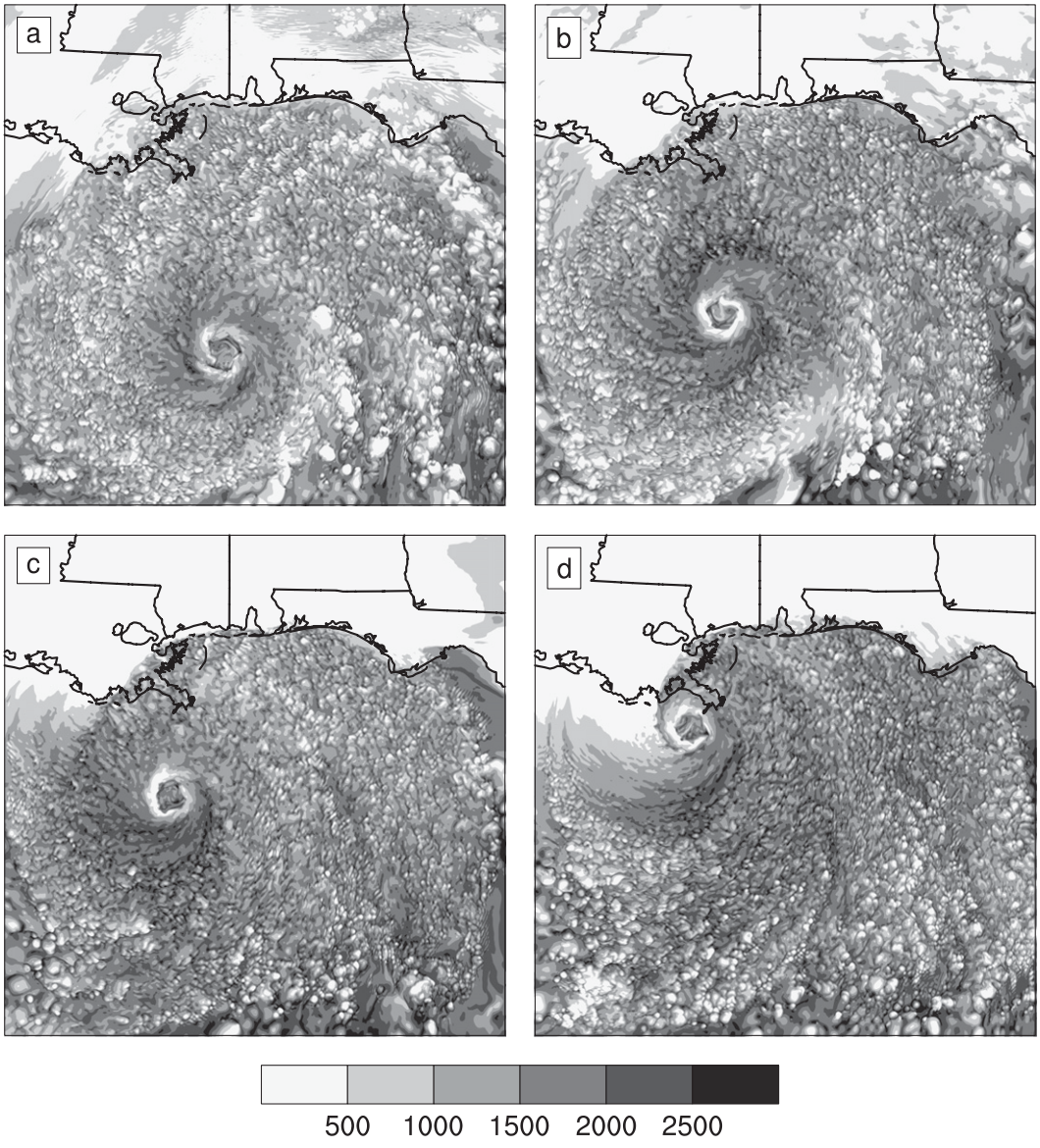

FIG. 13. Simulated surface-based CAPE (J kg^{-1}) at model times (a) 1800 UTC 28 Aug and (b) 0000, (c) 0600, and (d) 1200 UTC 29 Aug.

interact with the coastal front and may ingest into its updraft considerable streamwise vorticity from the cool side of the boundary (Figs. 6b and 6d). The cell should begin to deteriorate as it moves farther into the stable low-level air over land (Markowski et al. 1998), as was the case in the Valparaiso tornado (Fig. 3).

b. Significance of midlevel dry air

The possible link between the intrusion of dry air into a TC and a subsequent tornado outbreak has been noted often (e.g., Hill et al. 1966; McCaul 1987; Curtis 2004). However, Baker et al. (2009) suggested that dry air restricted to the upper troposphere and/or the outer fringes of the TC would not provide the level of evaporative cooling and subsequent destabilization necessary for enhanced deep convection. Relative humidity less than 60% was absent from the right-front quadrant of the simulated TC beneath the 500-hPa level (not shown), unsurprising given the dense coverage of convection (Fig. 5b). Although the above results do not refute the notion that a dry-air intrusion is important to TC supercell development, no firm conclusions can be drawn from this simulation. The authors are aware of ongoing efforts by others (Morin et al. 2010) to determine the impacts of a dry-air intrusion on supercell development within a quasi-idealized TC.

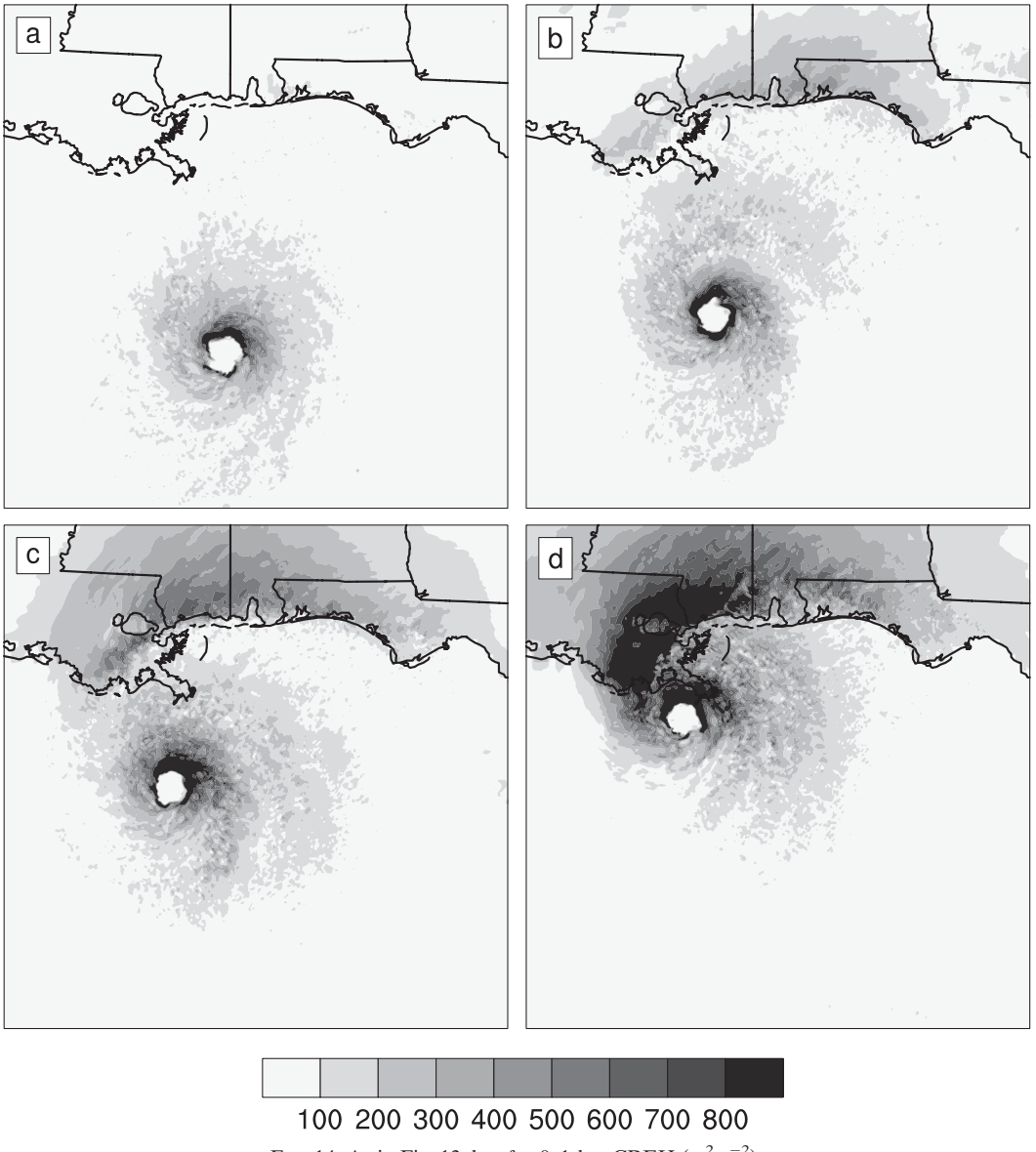

FIG. 14. As in Fig. 13, but for 0–1-km CREH (m^2 s^{-2}).

6. Concluding remarks

A high-resolution convection-permitting WRF simulation, along with radar and radiosonde observations, was used to investigate the multiscale environmental conditions conducive to supercell activities in the landfalling outer rainbands of Hurricane Katrina (2005). The salient results are as follows:

1) A surface baroclinic zone developed along the Gulf coast several hours before the center of the TC made landfall. Consistent with the results of Knupp et al. (2006), the approaching TC caused an extended period of coastal frontogenesis through a combination of confluence and differential diabatic heating.
2) This coastal front exhibited a strong influence on the distributions of CAPE and 0–1-km CREH—two parameters that are used to assess the potential for supercells and tornadoes. A coastal front also fits the ''buoyancy limiting'' or ''buoyancy-shear overlapping'' categories of baroclinic boundaries [which can promote tornadogenesis (Markowski et al. 1998)] that Edwards and Pietrycha (2006) associated with tornado outbreaks in other TCs. Indeed, a supercell in an outer rainband of Katrina intensified and spawned a tornado just onshore before quickly deteriorating farther inland.
3) Offshore, low-level helicity generally decreased away from the inner core of the TC, although within the

right-front/downshear-left/northeast quadrant, 0–1-km CREH greater than 100 $m^2 s^{-2}$ was observed in the outer rainbands. Surface-based CAPE was large across much of the Gulf of Mexico. These results are consistent with prior studies (e.g., Bogner et al. 2000; Molinari and Vollaro 2008, 2010; Baker et al. 2009; Eastin and Link 2009) that show favorable conditions for supercell formation within the outer rainbands well before TC landfall.

Although the recent increase in radar resolution should help identify reflectivity features such as hook echoes and inflow notches (e.g., Spratt et al. 1997; Schneider and Sharp 2007), there are many remaining challenges in forecasting TC tornado outbreaks. Radar imagery would help identify dry-air intrusions and associated enhancements of deep convection (Curtis 2004). We agree with Edwards and Pietrycha (2006) in their call for the use of more frequent surface mesoanalysis. Offshore buoy data could be incorporated to help identify coastal baroclinic zones, and those on radar duty should keep in mind that cells may change rapidly when moving onshore and/or crossing baroclinic boundaries.

Numerical modeling with even smaller grid spacing and/or ensembles should be considered for future work. Sensitivity experiments are necessary to determine the effects of various parameterizations—especially the planetary boundary layer scheme—on the formation of a coastal baroclinic zone. On a smaller scale, an updated version of McCaul and Weisman (1996) could be performed to determine how supercells develop offshore and evolve as they move inland. On the other hand, additional research will be needed to explore how predictable these miniature supercells are given the inherent chaotic nature of moist convection and the limit of predictability of the parent TCs (e.g., Sippel and Zhang 2008, 2010; Zhang and Sippel 2009).

Acknowledgments. We appreciate the valuable review comments provided by Da-Lin Zhang and three anonymous reviewers on earlier versions of the manuscript. We also thank Yonghui Weng for performing the WRF-EnKF analysis and simulations, and thank Michael Bell and Wen-Chau Lee for providing the dual-Doppler analysis used in Fig. 4. We benefited from discussions with Yvette Richardson, Thomas Hinson, Matt Parker, Lee, and Bell. This material is based upon work supported by a National Science Foundation (NSF) Graduate Research Fellowship under Grant DGE-0750756. Additional support is provided through NSF Grant ATM-0840651 and the NOAA Hurricane Forecast Improvement Project (HFIP).

REFERENCES

Akter, N., and K. Tsuboki, 2010: Characteristics of supercells in the rainband of numerically simulated Cyclone Sidr. *SOLA,* **6A,** 25–28, doi:10.2151/sola.6A-007.

Atkins, N. T., M. L. Weisman, and L. J. Wicker, 1999: The influence of preexisting boundaries on supercell evolution. *Mon. Wea. Rev.,* **127,** 2910–2927.

Baker, A. K., M. D. Parker, and M. D. Eastin, 2009: Environmental ingredients for supercells and tornadoes within Hurricane Ivan. *Wea. Forecasting,* **24,** 223–244.

Barnes, S. L., 1970: Some aspects of a severe, right-moving thunderstorm deduced from mesonetwork rawinsonde observations. *J. Atmos. Sci.,* **27,** 634–648.

Bluestein, H. B., 1993: *Observations and Theory of Weather Systems*. Vol. 2, *Synoptic–Dynamic Meteorology in Midlatitudes,* Oxford University Press, 594 pp.

Bogner, P. B., G. M. Barnes, and J. L. Franklin, 2000: Conditional instability and shear for six hurricanes over the Atlantic Ocean. *Wea. Forecasting,* **15,** 192–207.

Bunkers, M. J., B. A. Klimowski, J. W. Zeitler, R. L. Thompson, and M. L. Weisman, 2000: Predicting supercell motion using a new hodograph technique. *Wea. Forecasting,* **15,** 61–79.

Cressman, G. P., 1959: An operational objective analysis system. *Mon. Wea. Rev.,* **87,** 367–374.

Curtis, L., 2004: Midlevel dry intrusions as a factor in tornado outbreaks associated with landfalling tropical cyclones from the Atlantic and Gulf of Mexico. *Wea. Forecasting,* **19,** 411–427.

Davies-Jones, R. P., 1984: Streamwise vorticity: The origin of updraft rotation in supercell storms. *J. Atmos. Sci.,* **41,** 2991–3006.

——, 1993: Helicity trends in tornado outbreaks. Preprints, *17th Conf. on Severe Local Storms,* St. Louis, MO, Amer. Meteor. Soc., 56–60.

——, D. W. Burgess, and M. Foster, 1990: Test of helicity as a forecast parameter. Preprints, *16th Conf. on Severe Local Storms,* Kananaskis Park, AB, Canada, Amer. Meteor. Soc., 588–592.

Doswell, C. A., III, and E. N. Rasmussen, 1994: The effect of neglecting the virtual temperature correction on CAPE calculations. *Wea. Forecasting,* **9,** 625–629.

Eastin, M. D., and M. C. Link, 2009: Miniature supercells in an offshore outer rainband of Hurricane Ivan (2004). *Mon. Wea. Rev.,* **137,** 2081–2104.

Edwards, R., and A. E. Pietrycha, 2006: Archetypes for surface baroclinic boundaries influencing tropical cyclone tornado occurrences. Preprints, *23rd Conf. on Severe Local Storms,* St. Louis, MO, Amer. Meteor. Soc., P8.2. [Available online at http://ams.confex.com/ams/pdfpapers/114992.pdf.]

Emanuel, K. A., 1994: *Atmospheric Convection*. Oxford University Press, 580 pp.

Fang, J., and F. Zhang, 2010: Initial development and genesis of Hurricane Dolly (2008). *J. Atmos. Sci.,* **67,** 655–672.

——, and ——, 2011: Evolution of multiscale vortices in the development of Hurricane Dolly (2008). *J. Atmos. Sci.,* **68,** 103–122.

Frank, W. M., 1977: The structure and energetics of the tropical cyclone. I. Storm structure. *Mon. Wea. Rev.,* **105,** 1136–1150.

Gentry, R. C., 1983: Genesis of tornadoes associated with hurricanes. *Mon. Wea. Rev.,* **111,** 1793–1805.

Grell, G. A., and D. Devenyi, 2002: A generalized approach to parameterizing convection combining ensemble and data

assimilation techniques. *Geophys. Res. Lett.,* **29,** 1693, doi:10.1029/2002GL015311.

Hendricks, E. A., M. T. Montgomery, and C. A. Davis, 2004: The role of ''vortical'' hot towers in the formation of Tropical Cyclone Diana (1984). *J. Atmos. Sci.,* **61,** 1209–1232.

Hill, E. L., W. Malkin, and W. A. Schulz Jr., 1966: Tornadoes associated with cyclones of tropical origin—Practical features. *J. Appl. Meteor.,* **5,** 745–763.

Hong, S.-Y., J. Dudhia, and S.-H. Chen, 2004: A revised approach to ice microphysical processes for the parameterization of clouds and precipitation. *Mon. Wea. Rev.,* **132,** 103–120.

Kain, J. S., and Coauthors, 2008: Some practical considerations regarding horizontal resolution in the first generation of operational convection-allowing NWP. *Wea. Forecasting,* **23,** 931–952.

Knabb, R. D., J. R. Rhome, and D. P. Brown, 2006: Tropical cyclone report—Hurricane Katrina 23–30 August 2005. NOAA, 43 pp. [Available online at http://www.nhc.noaa.gov/pdf/TCR-AL122005_Katrina.pdf.]

Knupp, K. R., J. Walters, and M. Biggerstaff, 2006: Doppler profiler and radar observations of boundary layer variability during the landfall of Tropical Storm Gabrielle. *J. Atmos. Sci.,* **63,** 234–251.

Lee, W.-C., M. M. Bell, and K. E. Goodman Jr., 2008: Supercells and mesocyclones in the outer rainbands of Hurricane Katrina (2005). *Geophys. Res. Lett.,* **35,** L16803, doi:10.1029/2008GL034724.

Maddox, R. A., L. R. Hoxit, and C. F. Chappell, 1980: A study of tornadic thunderstorm interactions with thermal boundaries. *Mon. Wea. Rev.,* **108,** 322–336.

——, D. S. Zaras, P. L. MacKeen, J. J. Gourley, R. Rabin, and K. W. Howard, 1999: Echo height measurements with the WSR-88D: Use of data from one versus two radars. *Wea. Forecasting,* **14,** 455–460.

Malkin, W., and J. G. Galway, 1953: Tornadoes associated with hurricanes. *Mon. Wea. Rev.,* **81,** 299–303.

Markowski, P. M., E. N. Rasmussen, and J. M. Straka, 1998: The occurrence of tornadoes in supercells interacting with boundaries during VORTEX-95. *Wea. Forecasting,* **13,** 852–859.

——, C. Hannon, J. Frame, E. Lancaster, A. Pietrycha, R. Edwards, and R. L. Thompson, 2003: Characteristics of vertical wind profiles near supercells obtained from the Rapid Update Cycle. *Wea. Forecasting,* **18,** 1262–1272.

Mashiko, W., H. Niino, and T. Kato, 2009: Numerical simulation of tornadogenesis in an outer-rainband minisupercell of Typhoon Shanshan on 17 September 2006. *Mon. Wea. Rev.,* **137,** 4238–4260.

McCaul, E. W., Jr., 1987: Observations of the Hurricane ''Danny'' tornado outbreak of 16 August 1985. *Mon. Wea. Rev.,* **115,** 1206–1223.

——, 1991: Buoyancy and shear characteristics of hurricane–tornado environments. *Mon. Wea. Rev.,* **119,** 1954–1978.

——, and M. L. Weisman, 1996: Simulations of shallow supercell storms in landfalling hurricane environments. *Mon. Wea. Rev.,* **124,** 408–429.

——, D. E. Buechler, S. J. Goodman, and M. Cammarata, 2004: Doppler radar and lightning network observations of a severe outbreak of tropical cyclone tornadoes. *Mon. Wea. Rev.,* **132,** 1747–1763.

Meng, Z., and F. Zhang, 2008a: Tests of an ensemble Kalman filter for mesoscale and regional-scale data assimilation. Part III: Comparison with 3DVAR in a real-data case study. *Mon. Wea. Rev.,* **136,** 522–540.

——, and ——, 2008b: Tests of an ensemble Kalman filter for mesoscale and regional-scale data assimilation. Part IV: Comparison with 3DVAR in a month-long experiment. *Mon. Wea. Rev.,* **136,** 3671–3682.

Molinari, J., and D. Vollaro, 2008: Extreme helicity and intense convective towers in Hurricane Bonnie. *Mon. Wea. Rev.,* **136,** 4355–4372.

——, and ——, 2010: Distribution of helicity, CAPE, and shear in tropical cyclones. *J. Atmos. Sci.,* **67,** 274–284.

Montgomery, M. T., M. E. Nicholls, T. A. Cram, and A. B. Saunders, 2006: A vortical hot tower route to tropical cyclogenesis. *J. Atmos. Sci.,* **63,** 355–386.

Morin, M. J., M. D. Parker, K. A. Hill, and G. M. Lackmann, 2010: A numerical investigation of supercells in landfalling tropical cyclones. *Extended Abstracts, 25th Conf. on Severe Local Storms,* Denver, CO, Amer. Meteor. Soc., P3.3. [Available online at http://ams.confex.com/ams/pdfpapers/175965.pdf.]

NCDC, 2005: *Storm Data*. Vol. 47, No. 8, 318 pp.

NOAA, 2006: WSR-88D products and algorithms. Part C, *Federal Meteorological Handbook No. 11: Doppler Radar Meteorological Observations,* Office of Federal Coordinator for Meteorology, FCM-H11C-2006, 390 pp.

Noh, Y., W.-G. Cheon, S.-Y. Hong, and S. Raasch, 2003: Improvement of the K-profile model for the planetary boundary layer based on large eddy simulation data. *Bound.-Layer Meteor.,* **107,** 401–427.

Novlan, D. J., 1973: Hurricane spawned tornadoes. Dept. of Atmos. Sci. Rep. 200, Colorado State University, 57 pp. [Available online at http://digitool.library.colostate.edu/exlibris/dtl/d3_1/apache_media/2235.pdf.]

——, and W. M. Gray, 1974: Hurricane-spawned tornadoes. *Mon. Wea. Rev.,* **102,** 476–488.

Orton, R., 1970: Tornadoes associated with Hurricane Beulah on September 19–23, 1967. *Mon. Wea. Rev.,* **98,** 541–547.

Pearson, A. D., and A. F. Sadowski, 1965: Hurricane-induced tornadoes and their distribution. *Mon. Wea. Rev.,* **93,** 461–464.

Powell, M. D., 1982: The transition of the Hurricane Frederic boundary-layer wind field from the open Gulf of Mexico to landfall. *Mon. Wea. Rev.,* **110,** 1912–1932.

Ramsay, H. A., and C. A. Doswell III, 2005: A sensitivity study of hodograph-based methods for estimating supercell motion. *Wea. Forecasting,* **20,** 954–970.

Rao, G. V., J. W. Scheck, R. Edwards, and J. T. Schaefer, 2005: Structures of mesocirculations producing tornadoes associated with Tropical Cyclone Frances (1998). *Pure Appl. Geophys.,* **162,** 1627–1641.

Rasmussen, E. N., 2003: Refined supercell and tornado forecast parameters. *Wea. Forecasting,* **18,** 530–535.

——, S. Richardson, J. M. Straka, P. M. Markowski, and D. O. Blanchard, 2000: The association of significant tornadoes with a baroclinic boundary on 2 June 1995. *Mon. Wea. Rev.,* **128,** 174–191.

Sadowski, A., 1962: Tornadoes associated with Hurricane Carla, 1961. *Mon. Wea. Rev.,* **90,** 514–516.

Schneider, D., and S. Sharp, 2007: Radar signatures of tropical cyclone tornadoes in central North Carolina. *Wea. Forecasting,* **22,** 278–286.

Schultz, L. A., and D. J. Cecil, 2009: Tropical cyclone tornadoes, 1950–2007. *Mon. Wea. Rev.,* **137,** 3471–3484.

Sheets, R. C., 1969: Some mean hurricane soundings. *J. Appl. Meteor.,* **8,** 134–146.

Sippel, J. A., and F. Zhang, 2008: A probabilistic analysis of the dynamics and predictability of tropical cyclogenesis. *J. Atmos. Sci.,* **65,** 3440–3459.

——, and ——, 2010: Factors affecting the predictability of Hurricane Humberto (2007). *J. Atmos. Sci.,* **67,** 1759–1778.

Skamarock, W. C., J. B. Klemp, J. Dudhia, D. O. Gill, D. M. Barker, W. Wang, and J. G. Powers, 2005: A description of the Advanced Research WRF version 2. NCAR Tech. Note NCAR/TN-468+STR, 88 pp.

Smith, J. S., 1965: The hurricane-tornado. *Mon. Wea. Rev.,* **93,** 453–459.

Spratt, S. M., D. W. Sharp, P. Welsh, A. Sandrik, F. Alsheimer, and C. Paxton, 1997: A WSR-88D assessment of tropical cyclone outer rainband tornadoes. *Wea. Forecasting,* **12,** 479–501.

Srock, A. F., and L. F. Bosart, 2009: Heavy precipitation associated with southern Appalachian cold-air damming and Carolina coastal frontogenesis in advance of weak landfalling Tropical Storm Marco (1990). *Mon. Wea. Rev.,* **137,** 2448–2470.

Suzuki, O., H. Niino, H. Ohno, and H. Nirasawa, 2000: Tornado-producing mini supercells associated with Typhoon 9019. *Mon. Wea. Rev.,* **128,** 1868–1882.

Thompson, R. L., R. Edwards, J. A. Hart, K. L. Elmore, and P. Markowski, 2003: Close proximity soundings within supercell environments obtained from the Rapid Update Cycle. *Wea. Forecasting,* **18,** 1243–1261.

Weng, Y., and F. Zhang, 2012: Assimilating airborne Doppler radar observations with an ensemble Kalman filter for convection-permitting hurricane initialization and prediction: Katrina (2005). *Mon. Wea. Rev.,* in press.

Zhang, F., and J. A. Sippel, 2009: Effects of moist convection on hurricane predictability. *J. Atmos. Sci.,* **66,** 1944–1961.